

Video-rate fluorescence diffuse optical tomography for *in vivo* sentinel lymph node imaging

Metasebya Solomon,^{1,2} Brian R. White,^{2,3} Ralph E. Nothdruff,² Walter Akers,² Gail Sudlow,² Adam T. Eggebrecht,² Samuel Achilefu,^{1,2} and Joseph P. Culver^{1,2,3}

¹Department of Biomedical Engineering, Washington University, St. Louis, MO 63110, USA

²Department of Radiology, Washington University School of Medicine, St. Louis, MO 63110, USA

³Department of Physics, Washington University, St. Louis, MO 63110, USA

*culverj@mir.wustl.edu

Abstract: We have developed a fiber-based, video-rate fluorescence diffuse optical tomography (DOT) system for noninvasive *in vivo* sentinel lymph node (SLN) mapping. Concurrent acquisition of fluorescence and reference signals allowed the efficient generation of ratio-metric data for 3D image reconstruction. Accurate depth localization and high sensitivity to fluorescent targets were established in to depths of >10 mm. *In vivo* accumulation of indocyanine green (ICG) dye was imaged in the region of the SLN following intradermal injection into the forepaw of rats. These results suggest that video-rate fluorescence DOT has significant potential as a clinical tool for noninvasive mapping of SLN.

©2011 Optical Society of America

OCIS codes: (170.0170) Medical optics and biotechnology; (170.6510) Spectroscopy, tissue diagnostics; (170.3880) Medical and biological imaging; (170.5270) Photon density waves; (170.3660) Light propagation in tissues

References and links

1. T. M. Tuttle, M. Colbert, R. Christensen, K. J. Ose, T. Jones, R. Wetherille, J. Friedman, K. Swenson, and K. M. McMasters, "Subareolar injection of 99mTc facilitates sentinel lymph node identification," *Ann. Surg. Oncol.* **9**(1), 77–81 (2002).
2. T. Hojo, T. Nagao, M. Kikuyama, S. Akashi, and T. Kinoshita, "Evaluation of sentinel node biopsy by combined fluorescent and dye method and lymph flow for breast cancer," *Breast* **19**(3), 210–213 (2010).
3. V. Ntziachristos and R. Weissleder, "Charge-coupled-device based scanner for tomography of fluorescent near-infrared probes in turbid media," *Med. Phys.* **29**(5), 803–809 (2002).
4. S. V. Patwardhan, S. R. Bloch, S. Achilefu, and J. P. Culver, "Time-dependent whole-body fluorescence tomography of probe bio-distributions in mice," *Opt. Express* **13**(7), 2564–2577 (2005).
5. S. V. Patwardhan and J. P. Culver, "Quantitative diffuse optical tomography for small animals using an ultrafast gated image intensifier," *J. Biomed. Opt.* **13**(1), 011009 (2008).
6. V. Ntziachristos and R. Weissleder, "Experimental three-dimensional fluorescence reconstruction of diffuse media by use of a normalized Born approximation," *Opt. Lett.* **26**(12), 893–895 (2001).
7. V. Ntziachristos, G. Turner, J. Dunham, S. Windsor, A. Soubret, J. Ripoll, and H. A. Shih, "Planar fluorescence imaging using normalized data," *J. Biomed. Opt.* **10**(6), 064007 (2005).
8. J. P. Culver, A. M. Siegel, J. J. Stott, and D. A. Boas, "Volumetric diffuse optical tomography of brain activity," *Opt. Lett.* **28**(21), 2061–2063 (2003).
9. M. A. Franceschini and D. A. Boas, "Noninvasive measurement of neuronal activity with near-infrared optical imaging," *Neuroimage* **21**(1), 372–386 (2004).
10. B. W. Zeff, B. R. White, H. Dehghani, B. L. Schlaggar, and J. P. Culver, "Retinotopic mapping of adult human visual cortex with high-density diffuse optical tomography," *Proc. Natl. Acad. Sci. U.S.A.* **104**(29), 12169–12174 (2007).
11. G. Marquez, L. V. Wang, S. P. Lin, J. A. Schwartz, and S. L. Thomsen, "Anisotropy in the absorption and scattering spectra of chicken breast tissue," *Appl. Opt.* **37**(4), 798–804 (1998).
12. A. M. Nilsson, R. Berg, and S. Andersson-Engels, "Measurements of the optical properties of tissue in conjunction with photodynamic therapy," *Appl. Opt.* **34**(21), 4609–4619 (1995).
13. W. F. Cheong, S. A. Prahl, and A. J. Welch, "A Review of the Optical-Properties of Biological Tissues," *IEEE J. Quantum Electron.* **26**(12), 2166–2185 (1990).

14. S. T. Flock, S. L. Jacques, B. C. Wilson, W. M. Star, and M. J. C. van Gemert, "Optical properties of Intralipid: a phantom medium for light propagation studies," *Lasers Surg. Med.* **12**(5), 510–519 (1992).
15. A. N. Bashkatov, E. A. Genina, I. V. Korovina, V. I. Kochubey, Yu. P. Sinichkin, and V. V. Tuchin, "*In vivo* and *in vitro* study of control of rat skin optical properties by acting of osmotical liquid," *Proc. SPIE* **4224**, 300–311 (2000).
16. J. V. Frangioni, S. W. Kim, S. Ohnishi, S. Kim, and M. G. Bawendi, "Sentinel lymph node mapping with type-II quantum dots," *Methods Mol. Biol.* **374**, 147–159 (2007).
17. S. T. Proulx, P. Luciani, S. Derzi, M. Rinderknecht, V. Mumprecht, J. C. Leroux, and M. Detmar, "Quantitative imaging of lymphatic function with liposomal indocyanine green," *Cancer Res.* **70**(18), 7053–7062 (2010).
18. R. Sharma, W. Wang, J. C. Rasmussen, A. Joshi, J. P. Houston, K. E. Adams, A. Cameron, S. Ke, S. Kwon, M. E. Mawad, and E. M. Sevick-Muraca, "Quantitative imaging of lymph function," *Am. J. Physiol. Heart Circ. Physiol.* **292**(6), H3109–H3118 (2007).
19. E. M. Sevick-Muraca, R. Sharma, J. C. Rasmussen, M. V. Marshall, J. A. Wendt, H. Q. Pham, E. Bonefas, J. P. Houston, L. Sampath, K. E. Adams, D. K. Blanchard, R. E. Fisher, S. B. Chiang, R. Elledge, and M. E. Mawad, "Imaging of lymph flow in breast cancer patients after microdose administration of a near-infrared fluorophore: feasibility study," *Radiology* **246**(3), 734–741 (2008).
20. S. L. Troyan, V. Kianzad, S. L. Gibbs-Strauss, S. Gioux, A. Matsui, R. Oketokoun, L. Ngo, A. Khamene, F. Azar, and J. V. Frangioni, "The FLARE intraoperative near-infrared fluorescence imaging system: a first-in-human clinical trial in breast cancer sentinel lymph node mapping," *Ann. Surg. Oncol.* **16**(10), 2943–2952 (2009).
21. L. Sampath, W. Wang, and E. M. Sevick-Muraca, "Near infrared fluorescent optical imaging for nodal staging," *J. Biomed. Opt.* **13**(4), 041312 (2008).
22. R. Sharma, J. A. Wendt, J. C. Rasmussen, K. E. Adams, M. V. Marshall, and E. M. Sevick-Muraca, "New horizons for imaging lymphatic function," *Ann. N. Y. Acad. Sci.* **1131**(1), 13–36 (2008).
23. B. T. Lee, M. Hutteman, S. Gioux, A. Stockdale, S. J. Lin, L. H. Ngo, and J. V. Frangioni, "The FLARE intraoperative near-infrared fluorescence imaging system: a first-in-human clinical trial in perforator flap breast reconstruction," *Plast. Reconstr. Surg.* **126**(5), 1472–1481 (2010).
24. X. Intes, V. Ntziachristos, J. P. Culver, A. Yodh, and B. Chance, "Projection access order in algebraic reconstruction technique for diffuse optical tomography," *Phys. Med. Biol.* **47**(1), N1–N10 (2002).
25. B. W. Pogue, S. P. Poplack, T. O. McBride, W. A. Wells, K. S. Osterman, U. L. Osterberg, and K. D. Paulsen, "Quantitative hemoglobin tomography with diffuse near-infrared spectroscopy: pilot results in the breast," *Radiology* **218**(1), 261–266 (2001).
26. J. P. Culver, R. Choe, M. J. Holboke, L. Zubkov, T. Durduran, A. Slemple, V. Ntziachristos, B. Chance, and A. G. Yodh, "Three-dimensional diffuse optical tomography in the parallel plane transmission geometry: evaluation of a hybrid frequency domain/continuous wave clinical system for breast imaging," *Med. Phys.* **30**(2), 235–247 (2003).
27. R. Choe, A. Corlu, K. Lee, T. Durduran, S. D. Konecky, M. Grosicka-Koptyra, S. R. Arridge, B. J. Czerniecki, D. L. Fraker, A. DeMichele, B. Chance, M. A. Rosen, and A. G. Yodh, "Diffuse optical tomography of breast cancer during neoadjuvant chemotherapy: a case study with comparison to MRI," *Med. Phys.* **32**(4), 1128–1139 (2005).
28. Q. Zhang, T. J. Brukilacchio, A. Li, J. J. Stott, T. Chaves, E. Hillman, T. Wu, M. Chorlton, E. Rafferty, R. H. Moore, D. B. Kopans, and D. A. Boas, "Coregistered tomographic x-ray and optical breast imaging: initial results," *J. Biomed. Opt.* **10**(2), 024033 (2005).
29. D. K. Joseph, T. J. Huppert, M. A. Franceschini, and D. A. Boas, "Diffuse optical tomography system to image brain activation with improved spatial resolution and validation with functional magnetic resonance imaging," *Appl. Opt.* **45**(31), 8142–8151 (2006).
30. T. Austin, A. P. Gibson, G. Branco, R. M. Yusof, S. R. Arridge, J. H. Meek, J. S. Wyatt, D. T. Delpy, and J. C. Hebden, "Three dimensional optical imaging of blood volume and oxygenation in the neonatal brain," *Neuroimage* **31**(4), 1426–1433 (2006).
31. B. W. Zeff, B. R. White, H. Deghani, B. L. Schlaggar, and J. P. Culver, "Retinotopic mapping of adult human visual cortex with high-density diffuse optical tomography," *Proc. Natl. Acad. Sci. U.S.A.* **104**(29), 12169–12174 (2007).
32. B. R. White, A. Z. Snyder, A. L. Cohen, S. E. Petersen, M. E. Raichle, B. L. Schlaggar, and J. P. Culver, "Resting-state functional connectivity in the human brain revealed with diffuse optical tomography," *Neuroimage* **47**(1), 148–156 (2009).
33. J. P. Culver, V. Ntziachristos, M. J. Holboke, and A. G. Yodh, "Optimization of optode arrangements for diffuse optical tomography: A singular-value analysis," *Opt. Lett.* **26**(10), 701–703 (2001).
34. W. Rzyman, O. M. Hagen, R. Dziadziuszko, G. Kobienska-Gulida, A. Karmolinski, M. I. Lothe, W. Paleczka, M. Murawski, T. Jastrzebski, A. Kopacz, J. Jassem, and J. Skokowski, "Blue-dye intraoperative sentinel lymph node mapping in early non-small cell lung cancer," *Eur. J. Surg. Oncol.* **32**(4), 462–465 (2006).
35. L. Cao, M. Breithaupt, and J. Peter, "Geometrical co-calibration of a tomographic optical system with CT for intrinsically co-registered imaging," *Phys. Med. Biol.* **55**(6), 1591–1606 (2010).
36. L. Cao and J. Peter, "Bayesian reconstruction strategy of fluorescence-mediated tomography using an integrated SPECT-CT-OT system," *Phys. Med. Biol.* **55**(9), 2693–2708 (2010).

37. A. Li, E. L. Miller, M. E. Kilmer, T. J. Brukilacchio, T. Chaves, J. Stott, Q. Zhang, T. Wu, M. Chorlton, R. H. Moore, D. B. Kopans, and D. A. Boas, "Tomographic optical breast imaging guided by three-dimensional mammography," *Appl. Opt.* **42**(25), 5181–5190 (2003).
 38. W. C. Barber, Y. Lin, O. Nalcioglu, J. S. Iwanczyk, N. E. Hartsough, and G. Gulsen, "Combined fluorescence and x-ray tomography for quantitative *in vivo* detection of fluorophore," *Technol. Cancer Res. Treat.* **9**(1), 45–52 (2010).
 39. Q. Zhu, T. Durduran, V. Ntziachristos, M. Holboke, and A. G. Yodh, "Imager that combines near-infrared diffusive light and ultrasound," *Opt. Lett.* **24**(15), 1050–1052 (1999).
 40. Q. Zhu, "Optical tomography with ultrasound localization: initial clinical results and technical challenges," *Technol. Cancer Res. Treat.* **4**(3), 235–244 (2005).
 41. Q. Zhu, E. B. Cronin, A. A. Currier, H. S. Vine, M. Huang, N. Chen, and C. Xu, "Benign versus malignant breast masses: optical differentiation with US-guided optical imaging reconstruction," *Radiology* **237**(1), 57–66 (2005).
-

1. Introduction

Sentinel lymph node biopsy (SLNB) is the current standard procedure used for prognostic staging of cancers and therapeutic guidance. SLNB is a minimally-invasive procedure that involves the removal of sentinel nodes (the first lymph nodes that receive drainage from the primary tumor) for nodal staging. The location of sentinel lymph nodes (SLNs) is routinely determined by injecting radioactive lymphophilic tracer dye intra-operatively around the tumor region. The lymphophilic tracer is commonly composed of a radioactive colloid and/or optical contrast methylene blue for visual guidance [1,2]. Due to safety issues, a non-invasive and non-ionizing method for imaging of metastatic lymph nodes and lymphangiogenesis would be preferred. Fluorescence diffuse optical tomography (DOT) is an emerging deep tissue (>3 mm) imaging technique that has great potential as an alternative to radioactive tracer analysis for noninvasive detection and imaging of the sentinel lymph node. While fluorescence DOT often operates on the time scales of minutes to hours, the method also has the potential for imaging at higher speeds above the respiratory and cardiac fluctuations, allowing it to capture pharmacokinetics and pharmacodynamics of diagnostic and therapeutic agents.

Currently, most fluorescence diffuse optical tomography systems are CCD camera-based systems that scan at relatively slow speeds (i.e., frame rates < 0.01 Hz). The slow speed is due in part to the method by which ratio-metric data is acquired. Excitation and emission light intensity profiles are imaged consecutively, which requires that an interference filter for blocking the excitation light to be mechanically inserted between the two scans [3–5]. Comparison of sequentially acquired excitation and emission light intensities improves image quality through the generation of a normalized ratio-metric data set [6,7]. However, the mechanical requirements of sequential scanning slow data collection and pose a challenge for real-time imaging. Alternatively, DOT systems developed to image functional absorption contrast have used time- or frequency-encoding of the illumination with broad spectral detection to image fast activities (>10 Hz) within the human brain. This style of DOT system replaces the CCD-camera acquisition with multiple photodiode detectors in order to take advantage of the high dynamic range and high speed of avalanche photodiodes (APDs) [8–10]. However, the discrete detector DOT approach has not yet been applied to ratio-metric data for fluorescence DOT.

Herein, we aim to improve upon current fluorescence DOT platforms by developing a system with expanded dynamic range and faster data acquisition rates. Our video-rate, fiber-based fluorescence DOT system design is built upon a previously published APD-based platform for high-speed DOT [10].

The source-detector grid is designed as a contact probe to pre-operatively identify SLNs near the tumor region after administration of a fluorescent contrast agent. Biopsy of SLNs would follow intra-operatively to enable further histological evaluation for the presence of metastatic cells. These studies with a non-specific, but approved, contrast agent ICG will set the stage for future work with more specific targeted contrast agents that fluoresce/activate in the presence of metastatic cells.

Fiber-based, video-rate fluorescence DOT could additionally improve the flexibility of imaging by adapting to varying tissue curvatures and performing simultaneous multiple point illumination and collection, thus increasing the imaging frame rate.

We demonstrate the feasibility of *in vivo* imaging of the dynamics of dye accumulation in the region of the sentinel lymph nodes and quantify the accuracy of depth localization and sensitivity in tissue-simulating phantoms. These results demonstrate that fiber-based, video-rate fluorescence DOT is a practical and powerful tool that is well suited to a wide array of potential imaging applications, ranging from sentinel lymph node mapping to monitoring cancer therapy progression.

2. Methods

The generation of ratiometric (fluorescence-to-reference) data for fluorescence DOT reconstructions has previously relied on sequentially acquired measurements where the source laser is kept at the excitation frequency while a band-pass filter in front of the detector alternates between allowing through excitation and emission (fluorescent) light. The detected excitation light is then used as a reference to normalize the measured fluorescence. The acquisition of such ratiometric data allows reconstructions using the normalized Born approximation, which can be implemented to quantify fluorochrome distribution. However, while the use of an excitation reference is customary, it is not required. The assumption that light at the excitation wavelength acts as a good reference inherently assumes similar optical properties at the two wavelengths. And, if this assumption is made, there is no reason why light at the fluorescence wavelength could not be used as a reference. With a CCD-based system, this would be impractical, as there would be no way to determine the difference between the fluorescent and reference light at the same wavelength. However, with APD-based detection, high speed allows the use of frequency-encoding regimens to separate out contributions from different sources. With this encoding scheme, there is no longer any need for the hardware-based temporal-encoding of switching a filter in and out of the light beam. This paradigm is the basis for the system presented here.

The fiber-based, video-rate fluorescence DOT system is composed of an alternating grid of 12 sources and 13 detectors. The source channels contain 785 nm (Thorlabs DL7140-201S) (3.5 mW) and 830 nm (Thorlabs HL8325G) (0.25 mW) laser diodes, with dedicated laser diode drivers and control lines for each source, allowing flexible software configurable source encoding (frequency- and time-encoding) (Fig. 1A). Light from the sources is coupled into 2.5

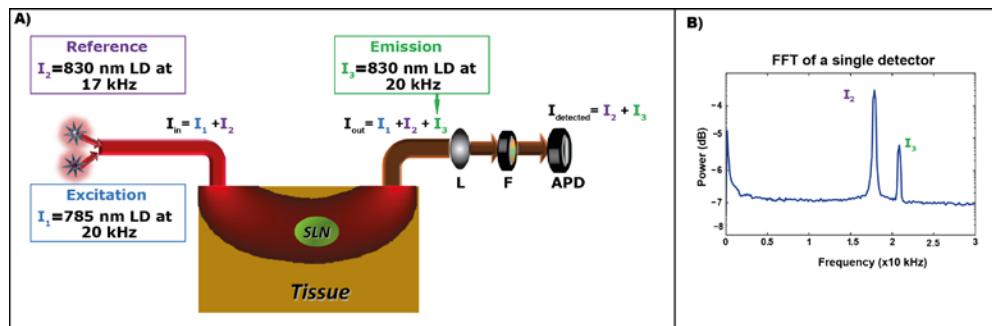


Fig. 1. Schematic of the video-rate fluorescence DOT hardware. (A) Schematic demonstrating frequency-encoding of 830 nm and 785 nm laser diode sources. Both reference and excitation light (at distinct frequencies) are incident on the tissue. Light exiting consists of reference, excitation, and emission (fluorescent) light. After collimation, the light is passed through a narrow band optical filter (F) to block the excitation light (785 nm). The resulting detected light, a sum of the reference transmission (I_2) and fluorescence emission (I_3), is simultaneously detected by a single detector. (B) A Fourier transform of the sum of I_2 and I_3 provides identification of transmission and emission signals from a single detector.

mm diameter fiber bundles. The detection channels use optically-filtered discrete avalanche photodiodes (Hamamatsu C5460-01) digitized with dedicated 24-bit analog-to-digital converters (MOTU HD 192). A narrowband optical filter with center wavelength 830 \pm 10 nm (CVI) and an out-of-band rejection of OD4 separates the excitation light from fluorescent and reference signals. An aspheric lens is used to collimate the light in order to optimize the blocking of excitation light by the narrowband interference filter and enhance fluorescent signal detection.

This design provides high instantaneous dynamic range (10^6) and cross-talk rejection (10^{-6}), so that light levels can be detected over many orders of magnitude. With this scheme, we acquire frequency-encoded fluorescence emission and reference transmission light levels simultaneously at each detector through the individual interference filters optimized for fluorescence emission (Fig. 1A). All data are acquired at a frame rate of 30 Hz. A total of 108 measurements from optode-pairs representing the 1st, 2nd, and 3rd nearest-neighbors are used for image reconstruction.

2.1. Ratiometric reconstruction

The reference transmission and fluorescent emission light intensities acquired concurrently at each detector (Fig. 1B) are used to generate ratio-metric data of fluorescence $\phi_{emi}(r_{s(i)}, r_{d(i)}, \lambda_{emi})$ divided by reference transmission $\phi_{ref}(r_{s(i)}, r_{d(i)}, \lambda_{ref})$. The data are then reconstructed using the normalized Born approach to correct for tissue and illumination inhomogeneities, which is written in discrete notation as $\mathbf{y} = \mathbf{A}\mathbf{x}$ with the following definitions [6].

In the Normalized Born approach $y_i = \frac{\phi_{emi}(r_{s(i)}, r_{d(i)}, \lambda_{emi})}{\phi_{ref}(r_{s(i)}, r_{d(i)}, \lambda_{ref})}$. When the bleed-through of the filter is accounted for, then the Normalized Born approach becomes

$$y_i = \frac{\phi_{emi}(r_{s(i)}, r_{d(i)}, \lambda_{emi}) - \phi_{bleedthrough}(r_{s(i)}, r_{d(i)})}{\phi_{ref}(r_{s(i)}, r_{d(i)}, \lambda_{ref})}$$

The ratiometric data (y) is generated by measuring the fluorescence light intensity profile $\phi_{emi}(r_{s(i)}, r_{d(i)}, \lambda_{emi})$ at emission wavelength, λ_{emi} , and the reference transmission light intensity profile, $\phi_{ref}(r_{s(i)}, r_{d(i)}, \lambda_{ref})$, at the reference wavelength, λ_{ref} . The i^{th} source-detector measurement (y_i) is associated with source ($r_{s(i)}$) and detector ($r_{d(i)}$) locations.

The bleed through measurement is made in the absence of a fluorescing agent and measures the amount of light leakage through the filter. It is determined by

$$\phi_{bleedthrough}(r_{s(i)}, r_{d(i)}) = \alpha \times \phi_{exc}(r_{s(i)}, \lambda_{exc}) = \alpha_{filter}^{d(i)} \times R \times \phi_{ref}(r_{s(i)}, \lambda_{ref}); \text{ where } R = \frac{\phi_{exc}(r_{s(i)}, \lambda_{exc})}{\phi_{ref}(r_{s(i)}, \lambda_{ref})};$$

α captures the optical density of the filter. In this fiber-based fluorescence DOT system there are individual detectors and sources, and the sources have separate lasers for both reference and excitation. Therefore, the α is calculated separately for each source-detector pairs. To calculate the bleedthrough specific to an imaging study we derived an estimate the bleedthrough of ϕ_{emi} based on ϕ_{ref} . Experimentally determined conversion factors (α and R) are used to account for the difference in power level between the excitation and reference lasers. R is measured using a power meter at source fiber tips of each sources, and $\alpha_{filter}^{d(i)}$ is the

excitation light measured with and without filter, $\phi_{exc}(r_{s(i)}, \lambda_{exc})$, for each detectors at the excitation wavelength (λ_{exc}) of 785 nm.

The sensitivity matrix ($A_{i,j}$) is created using the analytic solutions for photon density in the semi-infinite geometry to obtain the influence of a particular voxel j on every source and detector measurement i :

$$A_{i,j} = -\frac{s_o v h^3}{D_o} \frac{G(r_{s(i)}, r_j, \lambda_{ref}) G(r_j, r_{d(i)}, \lambda_{emi})}{G(r_{s(i)}, r_{d(i)}, \lambda_{ref})}; \quad x_j = \partial N_j$$

The S_o is calibration factor while h^3 represents the voxel volume. The D_o and v are the diffusion coefficient and speed of light in the medium. The two-point Green's function, G , models light transport for the given boundary condition. Optical properties at the reference wavelength of $\mu_a = 0.1 \text{ cm}^{-1}$ and $\mu'_s = 10 \text{ cm}^{-1}$ were used to model the optical properties of rat and chicken muscles for both *in vivo* and phantom studies [11–13]. In our case, a semi-infinite geometry is implemented. x_j is the j^{th} recovered image voxel that contains the fluorescence yield ∂N_j obtained using a Moore-Penrose generalized inverse [8].

2.2. Design of phantom studies

To evaluate the performance of the system, different concentrations of ICG targets in 3 mm diameter plastic tubes were prepared and embedded at 7 mm depth in a breast tissue mimicking phantom with $\mu_a = 0.1 \text{ cm}^{-1}$ and $\mu'_s = 10 \text{ cm}^{-1}$ (Fig. 2A). The breast tissue simulating phantom was constructed by mixing 1% Intralipid solution with Black India ink to obtain the appropriate absorption and scattering properties [14]. The absorption and reduced scattering coefficients are chosen based on previously published values of rats and chicken breast optical properties [11–13,15]. The targets contained solutions of indocyanine green (Sigma-Aldrich, St Louis, MO) in concentrations ranging from 1 nM to 1 μM . The averaged values from regions-of-interest (ROIs) of the reconstructed image were compared to known concentrations to evaluate the sensitivity and linear response of the system.

Analysis of the system's sensitivity as a function of depth was performed by submerging a 3 mm diameter plastic tube of 4 μM concentration in a tissue mimicking phantom. Starting at a depth of 5.5 mm, the tube was moved in 1.5 mm increments via a vertical stage until the middle of the tube reached a depth of 13.5 mm. The depth localization accuracy of the fluorescent target and sensitivity were calculated by averaging the intensity of the tube ROI and computing the center-of-mass for the different depths acquired.

2.3. Design of *in vivo* studies

We conducted a non-invasive preclinical study of fluorescent sentinel lymph node mapping in rats ($n = 5$) with our fiber-based, video-rate fluorescence DOT system. The hair was shaved from the axillary region prior to imaging. In order to test the translational feasibility of the system to humans (which will require imaging at depths $> 1 \text{ cm}$), we also conducted an experiment mimicking a deeper imaging scenario than would normally be available in a rat by inserting 8-10 mm of chicken breast tissue between the rat chest wall and the imaging pad (Fig. 2B). Imaging through 8-10 mm chicken breast increased the depth of the SLNs to 10-12 mm, which is deeper than the typical 2 mm where the SLNs are normally located below the skin surface in rats. Control images were acquired for 1 minute prior to administration of the ICG, and the dynamics of the injection in the axillary region were monitored for 10 minutes continuously.

Animal handling was performed according to the guidelines approved by the Washington University School of Medicine Animal Studies Committee for humane care and use of laboratory animals. For *in vivo* imaging, 50 μL of 100 μM ICG was injected intradermally in

the left forepaw of 200-250 g female Sprague Dawley rats (HSD, Indianapolis, IN) after giving a mixture of ketamine (85 mg/kg) and xylazine (15 mg/kg) for anesthesia. After imaging, rats were then euthanized with an overdose of pentobarbital solution (150 mg/kg, IP) and the lymph nodes were then resected for verification of ICG uptake.

For reference and verification of *ex vivo* ICG uptake by the lymph nodes, superficial fluorescence images were acquired without the layers of chicken breast using the Pearl near-infrared (NIR) fluorescence imaging system (LiCor Biosciences, Lincoln, NE).

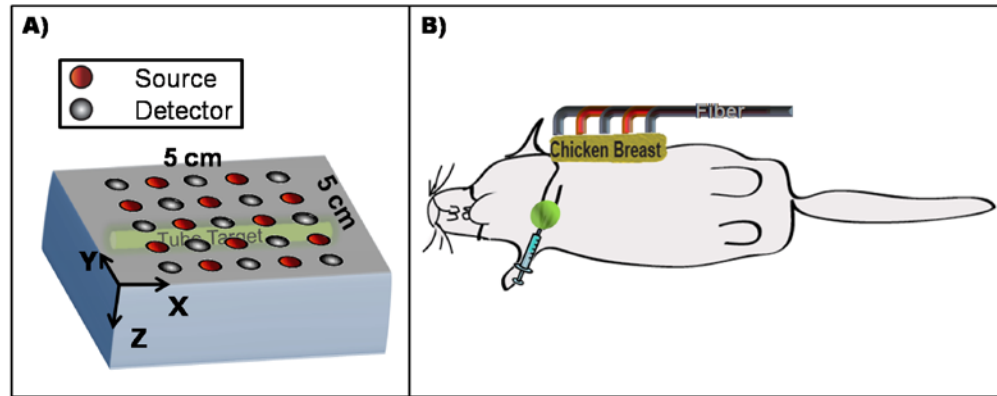


Fig. 2. Schematic of the video-rate fluorescence DOT experimental setup. (A) Schematic of our experimental setup with an imaging array and a 3 mm ICG tube embedded in a tissue mimicking phantom. (B) Schematic of the placement of the fiber array on a preclinical animal model using an 8-10 mm thick chicken breast to simulate a deep tissue imaging situation.

3. Results

3.1. System performance analysis with phantom studies

The Fourier transform of a measurement from a single detector illustrates the use of frequency-encoding to separate the emission and reference measurements acquired simultaneously (Fig. 1B). Following frequency-decoding, the intensities of both reference transmission and emission were retrieved. The data was then used to generate volumetric reconstructions of the fluorescence distribution. The reconstructed images from various depths suggest that our video-rate fluorescence DOT system has the capability to accurately section depths up to 13.5 mm (Fig. 3A). The resolution of the system was tested with simulated data for $1 \times 1 \times 1$ mm phantom targets at different depths. The size of the reconstructed perturbation is measured with the full width at half maximum (FWHM) of each target's reconstruction fluorescence profile. We observe a spatial broadening of the PSF with depth (Fig. 3B) with resolutions on the order of 12 mm. The center-of-masses (COMs) of the reconstructed fluorescence tubes (Fig. 3A) were computed by averaging the fluorescence intensity values for each experimental depth. The linear relationship between the experimental and the computed COMs demonstrate the depth localization accuracy up to 13.5 mm (Fig. 3C). The sensitivity as a function of depth was computed by taking the mean fluorescence intensity of the regions-of-interest from reconstructed image for the different depths acquired (Fig. 3D). The data demonstrate that the signal intensity drops exponentially with depth, as expected.

The relationship between the true dye concentration and the reconstructed voxel value (arbitrary units), is shown in Fig. 3E. The graph confirms the high dynamic range and linear response of our system to varying ICG concentrations as measured by the resulting fluorescent yield from 1 nM to 1 μ M. Values from this phantom analysis are used to generate a calibration factor for our *in vivo* studies.

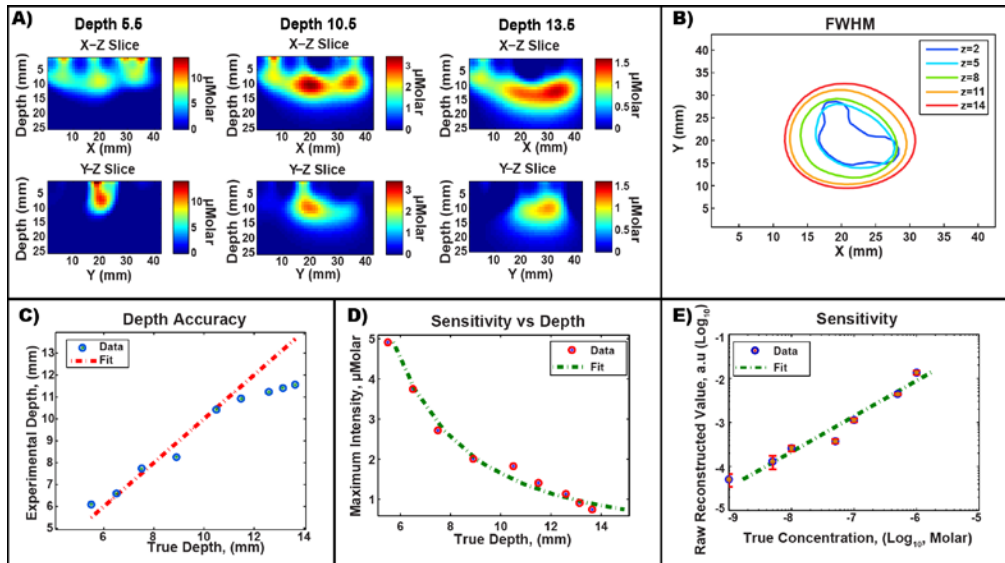


Fig. 3. System sensitivity analysis with phantom studies. (A) Vertical x-z and y-z slices of reconstructed experimental data from a fluorescent 3 mm tube target whose center of mass is located at 7.5 mm, 10.5 mm, and 13.5 mm depths. The system accurately reconstructs the tube shape with some artifact at the optode positions. (B) Point-spread function analysis using a simulated image reconstruction. Half-maximum contours of responses for different depths are shown. (C) Evaluation of the depth localization accuracy of a phantom target. The system has accurate localization from 6 to 13.5 mm. (D) Sensitivity vs depth. The data demonstrate that the signal intensity falls off exponentially with depth. (E) The relation between the raw reconstructed value and the true concentration of the dye was characterized by titration of ICG from 1 nM to 1 μ M concentrations in a 3 mm tube.

3.2. *In vivo* imaging of the uptake of dye into SLNs

We performed a pre-clinical *in vivo* study to evaluate the feasibility of imaging sentinel lymph nodes in rats noninvasively. ICG was injected intradermally into the forpaw and the axillary region was imaged with DOT. The DOT images of fluorescent lymph dynamics shown at 2 mm were obtained following injection of the ICG (Fig. 4A) (Media 1). Representative dynamics of fluorescent lymphatic fluid accumulation is obtained from a volume of about 30 mm³ from the region of the sentinel lymph node of the injection site (Fig. 4B). The mean of the background pixels shows no fluctuation associated with the dynamics of fluorescent dye.

Reflectance fluorescence images were captured using the Pearl NIR fluorescence imaging system before sacrificing the animal to confirm the DOT results (Fig. 4C). Reflectance fluorescence images acquired after euthanasia and removal of overlying skin further confirmed ICG uptake by the lymph node imaged by DOT (inset on Fig. 4D).

We repeated the experiment with an increased imaging depth by inserting 8-10 mm of chicken breast between the rats ($n = 5$) and the imaging pad. DOT images of fluorescent lymph dynamics were acquired and show that high quality imaging can be obtained even at increased depth (Fig. 5A) (Media 2). Time courses of the SLN region as well as background pixels demonstrate the representative dynamics of fluorescent lymphatic fluid accumulation after the injection (in two individual rats Fig. 5B and averaged over all five rats Fig. 5C). The variability in the lymph dynamics and accumulation in the SLNs can be associated with inter- and intra-subject variability of the periodic expansion and contraction structures that surrounds the lymphatic vessels. The results demonstrate the potential of the video-rate fluorescence DOT system to image the *in vivo* dynamics of dye accumulation in SLNs.

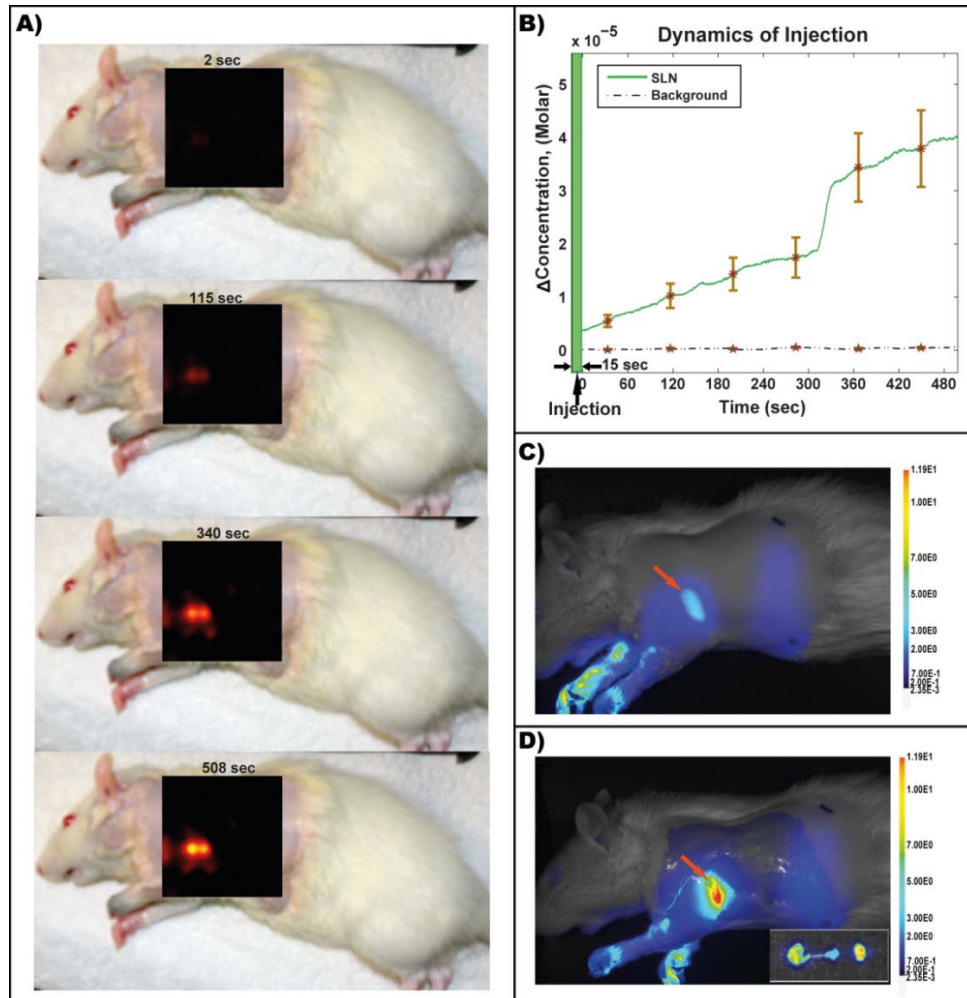


Fig. 4. Shallow imaging of lymph dynamics. (A) DOT images of the fluorescence dynamics at 2 mm depth in a rat following injection of ICG into the left forepaw. (B) Time traces of the dynamics of ICG accumulation in the region of the sentinel lymph node (for comparison the mean background signal is shown). (C) Reflectance fluorescent imaging of the sentinel lymph node region demonstrating fluorescence from the injection site (paws) and the lymph vessels leading to axillary lymph nodes (arrow). (D) Reflectance fluorescent image of the rat after euthanasia and removal of overlying skin. Inset: fluorescence from *ex vivo* imaging shows ICG uptake in the lymph nodes.

4. Discussion

Fiber-based, video-rate fluorescence DOT has the potential to become a powerful and practical tool for a broad array of imaging applications, ranging from sentinel lymph node mapping to monitoring cancer therapy progress. We demonstrated the feasibility of a 30 Hz APD-based fluorescence DOT system. Images of fluorescent targets in tissue mimicking phantoms were used to confirm the high dynamic range and linear response of the system and the accurate localization of targets in the range of depths from 5.5 to 13.5 mm. As the optical properties used in our experiments are higher than those reported for human breast tissues we expect the depth sensitivity and dynamic range to be improved in human studies.

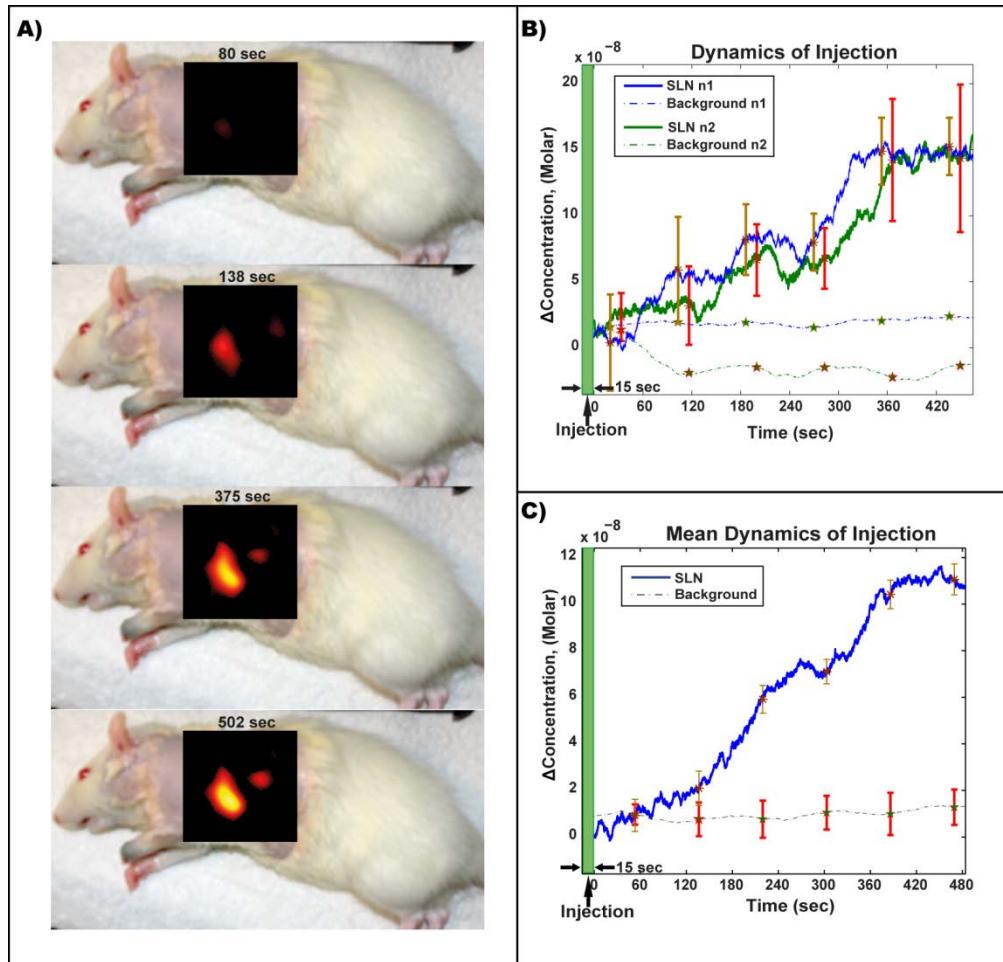


Fig. 5. Deep (>10 mm) imaging of lymph dynamics. The video rate fluorescence DOT was used to image the SLN region in rats through 8-10 mm of chicken breast following ICG injection into the rat forepaw. (A) The dynamics in a slice at 11 mm depth from a DOT reconstruction. (B) Time traces of the dynamics (for 2 representative rats) of a region around the SLN and of the mean of all background pixels. (C) Dynamics of ICG accumulation averaged over 5 rats.

We also successfully demonstrated the *in vivo* capabilities of the system by noninvasively imaging the dynamics of ICG accumulation in a rat. Accumulated dye in the region of the sentinel lymph nodes was imaged to a depth of 10-12 mm over a 10 minute time course. These results demonstrate the potential for imaging the pharmacokinetics of fluorescent diagnostic and therapeutic agents.

Previous two-dimensional fluorescence reflectance imaging (FRI) has been used to image lymph nodes and the lymphatic systems in animal models and cancer patients [16–22]. For instance, the lymph dynamics and lymph node images obtained after injection of ICG in breast cancer patients show the feasibility of implementing FRI for nodal staging [19]. The specificity of the FRI method was further evaluated with an intraoperative FRI system by localizing the same SLNs as lymphoscintigraphy in breast cancer patients [20]. This particular FRI system is currently on clinical trials for intraoperative SLN mapping in cancer patients [16,17,20,23]. While the FRI method is useful, its sensitivity declines quickly with imaging depth.

Three-dimensional DOT methods address several limitations of FRI and can potentially improve deep-tissue sensitivity, volumetric localization, resolution, and quantitative accuracy. For example, DOT approaches have been used in small animals to image whole bodies [4,24] and in humans to image breast [25–28] and brain [29–31] tissues at depths of several centimeters. One limitation of our current system for application in humans is the limited field of view. The potential for an expanded system with up to 48 sources and 48 detectors has been demonstrated for brain imaging [32]. A higher density imaging array could also potentially increase the resolution, particularly at the shallower depths [33].

Sentinel lymph node localization is currently performed by administering radiocolloids conjugated with blue dye for intraoperative guidance [34]. The potential of implementing other organic optical dyes such as fluorescein and indocyanine green has also been demonstrated in multiple clinical trials [2,17,19–21,23]. Extensive research is still needed into targeted optical dyes. Fiber-based, video-rate fluorescence DOT aided with targeted optical dyes could have the potential to assess the cancer status of SLNs non-invasively in order to avoid unnecessary surgical procedures.

Multimodal imaging with fluorescence DOT could also play an important role in the detection and imaging of sentinel lymph nodes for cancer management. DOT could be combined with, for example, nuclear imaging to improve the accuracy of DOT images during data processing and image reconstruction [35–38]. In addition to a standalone mode (and due to the flexibility of the fiber array geometries), video-rate fluorescence DOT also has the potential to be combined with handheld ultrasound (US) and/or photoacoustic tomography (PAT). Fibers assembled around the periphery of the PAT/US imaging head could provide many tracings through the PAT/US imaging volume. A similar approach wherein DOT is combined with ultrasound has been demonstrated feasible for imaging breast cancer [39–41]. In these scenarios, the fluorescence molecular contrast of DOT would complement the high resolution function and anatomical data of PAT and US.

5. Conclusion

We have developed a fiber-based, video-rate fluorescence DOT system and demonstrated its potential for *in vivo* imaging. We demonstrated that a 30 Hz APD-based DOT system can be operated in fluorescence mode. A fiber-based imaging array was used to image a fluorescent target within an agarose phantom and to exhibit our system's high sensitivity. These results confirmed the high dynamic range and linear response of the system and accurate localization of various depths. We have also successfully demonstrated the capability of the system for sentinel lymph node mapping in rats. Further progress with this technology has the potential to provide a useful clinical tool for a wide array of imaging applications, ranging from sentinel lymph node mapping to monitoring cancer therapy progress.

Acknowledgments

This research was supported in part by the Network for Translational Research U54CA136398 TSP-3 (Culver) and U54CA136398 TSP-1(Achilefu). Dr. Akers is supported by an award from the National Center for Research Resources (K01RR026095).